

# Magnetic orders, excitations, and phase transitions in $\text{Fe}_{1+y}\text{Te}$

G. Chen, S. Choi, and L. Radzihovsky

*Department of Physics, University of Colorado, Boulder, CO, 80309-0390, U.S.A.*

(Dated: April 23, 2022)

We study the magnetic properties of  $\text{Fe}_{1+y}\text{Te}$ , a parent compound of the iron-based high-temperature superconductors. Motivated by recent neutron scattering experiments, we show that a spin  $S = 1$  exchange model, supplemented by a single-ion spin anisotropy, accounts well for the experimentally observed low temperature magnetic phase diagram, that exhibits a commensurate bicollinear order at low Fe dopings ( $y \lesssim 0.12$ ) and an incommensurate spin-spiral order at high Fe dopings ( $y \gtrsim 0.12$ ). We suggest that the commensurate-incommensurate transition at  $y \simeq 0.12$  is due to the competition between the exchange interaction and the local spin anisotropy. At low Fe dopings, the single-ion spin anisotropy is strong and pins the spins along the easy axis, which, together with the spatially anisotropic exchanges, induces a unusual bicollinear commensurate magnetic order. The low-energy spin-wave excitation is gapped due to the explicit breaking of spin-rotational symmetry by the local spin anisotropy. At high Fe dopings, the single-ion anisotropy is weak, and the exchange favors an incommensurate coplanar state. The incommensurate magnetic wavevector averages out the spin anisotropy so that a gapless low-energy spin-wave excitation is obtained. We also analyze the low-energy hydrodynamic model and use it to describe the magneto-structural transition and the static and dynamical spin structure factors across the magnetic ordering transitions.

PACS numbers: 75.50.Ee, 74.70.-b, 71.10.-w, 71.70.Ej

## I. INTRODUCTION

Initiated by Hosono and co-worker's discovery of iron-based high-temperature superconductivity in fluorine-doped  $\text{LaOFeAs}$ ,<sup>1</sup> there have been tremendous research activities and developments in the area of iron-based superconductors. While searching for higher transition temperature and its mechanism, many classes of materials were discovered and analyzed extensively, theoretically and experimentally.<sup>2</sup> The most well-known materials are the 1111 (e.g.  $\text{LaOFeAs}$ ) and 122 (e.g.  $\text{BaFe}_2\text{As}_2$ ) compounds, conventionally referred to as iron arsenide materials.

These iron-based superconductor exhibit many interesting features that have attracted considerable attention.<sup>2</sup> Their phase diagram exhibits some similarities to that of cuprate superconductors, with the pairing mechanism that is believed to be unconventional (i.e., non-phonon mediated). Concomitant with this is the superconducting order parameter that is predicted to be (with some experimental evidence<sup>3,4</sup>) of an unconventional, extended ( $s_{++}$  and  $s_{\pm}$ , alternating sign around the Brillouin zone but fully gapped on the Fermi pockets)  $s$ -wave type. Angle resolved photoemission spectroscopy (ARPES) and inelastic neutron scattering studies suggest that the Fermi surface nesting accompanied by the spin density wave plays a central role for mediating the superconducting mechanism.

More recently discovered, the so-called 11 materials (e.g.  $\text{FeSe}$  and  $\text{FeTe}$  based compounds) also show superconductivity with doping of sulfur or selenium. Their simpler structure, with no atoms at the interplanar layer, is hoped to be present a simpler challenge of uncovering the nature of the pairing mechanism, but still to shed light more generally on iron-based and other strongly cor-

related superconductors.

With magnetism believed to be central to high temperature superconductivity and interesting in its own right, much attention has also recently turned to the magnetic parent compounds, such as the self-doped  $\text{Fe}_{1+y}\text{Te}$ .<sup>5-10</sup>  $\text{Fe}_{1+y}\text{Te}$  is observed to exhibit a number of novel characteristics (see Fig. 1). The most interesting of these is a unusual bicollinear antiferromagnetic (AFM) state, with a commensurate, planar spin-spiral order characterized by  $[\pi/2, -\pi/2]$  ordering wavevector. A first-order thermal transition to this state is accompanied by a structural transition to an orthorhombic state (with a slight monoclinicity) in low Fe doped samples.<sup>5</sup> At low temperatures the magnetic order also undergoes a commensurate to incommensurate transition with a critical iron doping at  $y_c \simeq 0.12$ , with low doping corresponding to the commensurate phase.<sup>6</sup>

Measurement of the spin susceptibility with a large magnetic moment of order  $2\mu_B$  (at 5K in a  $y = 0.068$  sample<sup>6</sup>) and no Fermi surface nesting observed in DFT<sup>7</sup> and ARPES<sup>8</sup> suggest that (despite its metallic nature) a local moment description may be sufficient to capture magnetism in  $\text{Fe}_{1+y}\text{Te}$  compounds. This is supported by first-principles electron structure calculations that observe the formation of the iron local moments.<sup>11,12</sup> There have also been several theoretical studies based on the local moment description.<sup>9-13</sup> Turner *et al.* assumed that the electrons are localized and the structural transition is driven by an orbital ordering resulting from Jahn-Teller coupling.<sup>9</sup> Their model consists of antiferromagnetic superexchange and ferromagnetic double exchange, which together favor an incommensurate (close to bicollinear) state, as well as a biquadratic exchange which can then drive the system to the commensurate bicollinear AFM state. Fang *et al.* also developed a local spin model with a rather complicated exchange interaction.<sup>10</sup> They ob-

tained a rich phase diagram that includes the two relevant phases observed in  $\text{Fe}_{1+y}\text{Te}$ . Yin *et al.* unified the two pictures based on itinerant electrons and localized moments in  $\text{Fe}_{1+y}\text{Te}$  in analogy with manganites.<sup>13,14</sup> They pointed out the sensitive competition between the superexchange and orbital-degenerate double-exchange ferromagnetism, finding several collinear states including the bicollinear AFM state. Although these models are claimed to obtain the bicollinear AFM and incommensurate spin-spiral states observed in  $\text{Fe}_{1+y}\text{Te}$ , the underlying spin-rotational symmetry in the spiral plane of these models predicts a gapless spin wave excitation, which is inconsistent with experimental observations of a gapped spectrum in the commensurate bicollinear AFM state for  $y \lesssim 0.12$ .<sup>15,16</sup>

The main experimental motivation for our theoretical study is the recent neutron scattering measurements on the  $\text{Fe}_{1+y}\text{Te}$  samples with a series of Fe dopings.<sup>5,15,17</sup> Besides being consistent with the schematic phase diagram in Fig. 1, the experimental findings provide additional information about the properties of different magnetic phases. In particular, in Parshall *et al.*'s experiment on a  $y = 0.08$  sample, it has been observed that an *incommensurate* inelastic peak (at the wavevector  $[0.45\pi, -0.45\pi]$ ) in the dynamical spin structure factor precipitously shifts to a commensurate position (at the wavevector  $[\pi/2, -\pi/2]$ ).<sup>18</sup> Moreover, a gapped spin-wave spectrum is observed in the dynamical spin structure factor for the samples with the bicollinear AFM order, while a gapless spin-wave spectrum is obtained for the samples with the incommensurate order.

To account for the previous and current experiments, we take the local moment description and consider a microscopic spin model for  $\text{Fe}_{1+y}\text{Te}$  in Sec. II. Clearly, a gapped spin-wave spectrum for the bicollinear AFM state suggests the explicit breaking of the spin rotational symmetry at the Hamiltonian level. Such a spin anisotropy is certainly allowed on symmetry grounds by the orthorhombic crystal structure in the ordered phase. Therefore, we introduce a *single-site spin anisotropy* for the localized  $S = 1$  spin moment. In addition, we choose the spin exchange introduced by Turner *et al.* but abandon the superfluous biquadratic exchange. The single-site spin anisotropy, together with the spin exchange, naturally generates the schematic phase diagram in Fig. 1. For the bicollinear AFM state at low Fe doping, the lattice distortion is large and the spin anisotropy is expected to be strong. The strong spin anisotropy favors collinear spin states. The spin exchange further selects the bicollinear AFM state observed in the experiment. The spin-wave spectrum of this state is found to be gapped. As the Fe doping is increased, the lattice distortion is reduced and the spin anisotropy is also expected to be reduced. In the end, the dominant spin exchange favors an incommensurate state. This incommensurate spin state averages out the local spin anisotropy, which effectively restores the spin-rotation symmetry and leads to a gapless spin-wave spectrum. We also provide a possible mi-

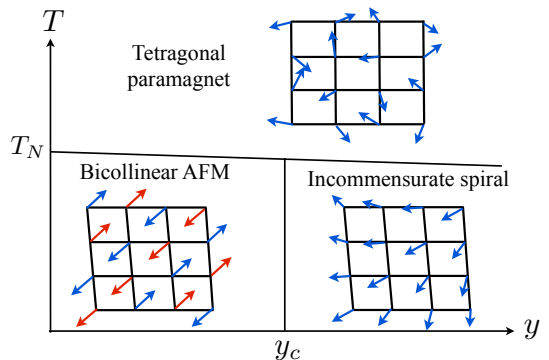


FIG. 1. The schematic temperature ( $T$ ) Fe-doping ( $y$ ) phase diagram for  $\text{Fe}_{1+y}\text{Te}$ .  $y_c \simeq 0.12$  and the critical temperature  $T_N \simeq 65\text{K}$ . In the magnetic ordered phase, the system has an orthorhombic crystal structure, and the incommensurate spiral is in the  $bc$  plane.

croscopic origin for the single-ion spin anisotropy by introducing the magnetoelastic coupling in Sec II E.

In Sec. III, we focus on a phenomenological continuum Landau theory and provide a mean-field analysis of the magnetostructural transition in  $\text{Fe}_{1+y}\text{Te}$ . We obtain a global phase diagram that includes both paramagnetic and AFM phases with tetragonal or orthorhombic structures. In Sec. IV, we then discuss the low temperature AFM phases of orthorhombic phase. With a proper parameterization of the magnetic order, we map the continuum theory to a sine-Gordon model and explain and analyze the commensurate-incommensurate transition from the bicollinear AFM state to the incommensurate AFM state upon Fe dopings, calculating the static spin structure factor near the transition.

In Sec. V, utilizing this continuum model of Sec. IV and general conservation and symmetry principles we propose a hydrodynamic theory (extensions of model E and F in the Halperin-Hohenberg classification<sup>19,20</sup>) for a finite temperature, low frequency, long wavelength description of the system. We use it to calculate the static and dynamical spin structure factors in different paramagnetic and magnetically ordered phases.

The rest of the paper is organized as follows. In Sec. II, we introduce the microscopic model that is an extension of the model in Ref. 9, incorporating a key new ingredient of single-ion spin anisotropy and omitting the superfluous biquadratic exchange. We use it to obtain the classical phase diagram and the low-energy magnetic excitation spectrum. We study the magnetostructural transition in Sec. III and discuss the commensurate-incommensurate transition in Sec. IV. In Sec. V, we compute the static and dynamical spin structure factors in the different magnetic phases. We conclude the paper in Sec. VI with a summary and discussion of our predictions.

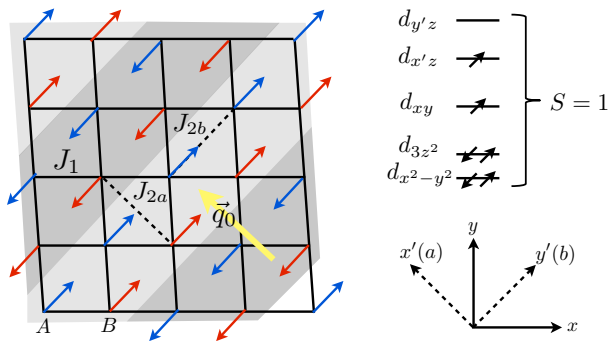


FIG. 2. Left: bicollinear AFM state with spins locked by the single-ion anisotropy to the  $b$  crystal axis, and exchange couplings of the model Eq. (1) indicated; upper right: the local electron configuration of  $\text{Fe}^{2+}$  in the orthorhombic phase; lower right: the choice of coordinates, with the  $c$ -axis out of the plane.

## II. MODEL OF FeTe

### A. Microscopic lattice model

Our microscopic model for  $\text{Fe}_{1+y}\text{Te}$  is based on the lattice  $S = 1$  exchange model introduced by Turner *et al.*<sup>9</sup> Although  $\text{Fe}_{1+y}\text{Te}$  compounds are metallic, we assume that the magnetism in  $\text{Fe}_{1+y}\text{Te}$  is described by localized  $S = 1$  spin moments. The main difference between our model and that of Ref. 9 is our introduction of the single-ion spin anisotropy that explicitly breaks spin-rotational symmetry, which is expected from the orthorhombic low-temperature crystal structure and the observed gapped spin-wave spectrum in the bicollinear AFM state in low Fe doped samples. Microscopically, the transition to the orthorhombic state can be argued to be associated with the orbital ordering via Jahn-Teller coupling.<sup>9</sup> However, we will capture it more simply, phenomenologically through a magnetoelastic coupling, that we analyze in Sec. III. Also in contrast to Ref. 9, we neglect the biquadratic exchange, that in our view is not necessary to capture the  $\text{Fe}_{1+y}\text{Te}$  phenomenology.

At low temperatures,  $\text{Fe}_{1+y}\text{Te}$  distorts from a tetragonal to a weakly monoclinic structure at low Fe dopings and to an orthorhombic structure at high Fe dopings. Since the monoclinic distortion is fairly weak, with  $\beta \simeq 89.2$  degrees,<sup>5</sup> we neglect it for simplicity and take the low temperature crystal structure to be orthorhombic for all Fe dopings. At low temperature orthorhombic phase, the crystal is elongated along  $a$  crystal axis and compressed along  $b$  crystal axis, *i.e.*  $a > b$ . Here  $a$  and  $b$  are lattice constants along corresponding lattice directions. As shown in Fig. 2, the orthorhombic distortion lifts the degeneracy of  $d_{y'z}$  and  $d_{x'z}$  orbitals of  $\text{Fe}^{2+}$  that is present in the high temperature tetragonal phase (with  $a = b$ ). The lower  $e_g$  doublets are both doubly occupied and the upper  $d_{xy}$  and  $d_{x'z}$  orbitals are singly occupied, forming a local spin moment  $S = 1$ .<sup>9</sup>

As discussed in Ref. 9, because of the single occupancy of  $d_{xy}$  and  $d_{x'z}$  orbitals, the exchange interaction,  $J_{2a}$ , along  $a$  (or equivalently  $x'$ ) axis is expected to be antiferromagnetic. On the other hand, along the  $b$  ( $y'$ ) axis that is more metallic we take to be ferromagnetic with exchange,  $J_{2b}$ , via a double exchange of the extra electron on the anisotropic upper  $d_{y'z}$  orbital due to Fe (self-) doping. Such ferromagnetic exchange can also arise from the nearly 90 degree exchange path.<sup>10</sup> In addition to next nearest neighbor (NNN) exchanges,  $J_{2a}$  and  $J_{2b}$ , we include an antiferromagnetic exchange  $J_1$  between nearest neighbors (NN), that for simplicity we take to be the same along  $x$  and  $y$  directions. The orthorhombic single-ion anisotropy is allowed by symmetry and microscopically arises from the second order contribution of the spin-orbit coupling. Thus, we take the full Hamiltonian to be

$$\mathcal{H} = J_1 \sum_{\langle ij \rangle} \mathbf{S}_i \cdot \mathbf{S}_j + J_{2a} \sum_{\langle\langle ij \rangle\rangle_a} \mathbf{S}_i \cdot \mathbf{S}_j - J_{2b} \sum_{\langle\langle ij \rangle\rangle_b} \mathbf{S}_i \cdot \mathbf{S}_j + \sum_i [D_a (S_i^a)^2 - D_b (S_i^b)^2], \quad (1)$$

in which, the last term is the single-ion spin anisotropy allowed by the orthorhombic symmetry, with  $D_a, D_b > 0$ , so that  $b$  is the easy axis. Because all the interesting spatial variation takes place in the  $ab$ -plane of FeTe, above and throughout the paper we focus on 2D case of a single plane.

We first treat this microscopic model classically, together with the linear spin-wave analysis appropriate at low temperature inside the ordered states. We supplement this with a hydrodynamic theory more appropriate at high temperatures in Sec. IV, that allows us to compute the dynamic structure factors measured via inelastic neutron scattering in Ref. 18.

### B. Mean field analysis

First we find the ground state of  $\mathcal{H}$  for a vanishing spin anisotropy,  $D_a = D_b = 0$ , treating spins classically. Straightforward calculation shows that the ground state is a coplanar spin spiral with

$$\mathbf{S}_i = S[\cos(\mathbf{k} \cdot \mathbf{r}_i)\hat{m}_1 + \sin(\mathbf{k} \cdot \mathbf{r}_i)\hat{m}_2], \quad (2)$$

where  $\hat{m}_1$  and  $\hat{m}_2$  are two orthogonal unit vectors and the ordering wavevector  $\mathbf{k} = [k_1, -k_1] = -k_1\hat{\mathbf{a}}$  with

$$\cos k_1 = -\frac{J_1}{2J_{2a}}. \quad (3)$$

Generically this spin spiral is incommensurate for  $\frac{J_1}{2J_{2a}} < 1$ . When  $\frac{J_1}{2J_{2a}} \geq 1$ , the ground state is the conventional  $[\pi, \pi]$  Néel state on the square lattice. Since in the experiments<sup>5,15,17,18</sup>  $k_1$  is observed to be very close to  $\pi/2$ , so we expect  $J_1 < J_{2a}$  in FeTe.

ground state	classical energy per site
commensurate	$-(J_{2a} + J_{2b} + D_b)S^2$
incommensurate	$-(J_{2a} + J_{2b} + \frac{J_1^2}{2J_{2a}} + \frac{D_b - D_a}{2})S^2$
Néel	$-(-J_{2a} + J_{2b} + 2J_1 + D_b)S^2$

TABLE I. The classical energies for three candidate ground states.  $S$  is the spin magnitude.

The inclusion of the spin anisotropy raises the competition between the exchange that favors the incommensurate spin-spiral state and the spin anisotropy that favors collinear states with spins aligned along the  $b$  axis. If  $J_1$  is small compared to  $J_{2a}$  and  $J_{2b}$ , the collinear states should have a ferromagnetic spin configuration along the  $b$  direction and an antiferromagnetic spin configuration along the  $a$  direction. The resulting collinear state turns out to be the bicollinear AFM state with the commensurate ordering wavevector  $[\pi/2, -\pi/2]$ . Moreover, for an incommensurate coplanar state, the spin anisotropy locks the spin spiral onto the easy  $bc$  plane. Furthermore, with the presence of the spin anisotropy the  $b$  and  $c$  directions are no longer equivalent, and the spin spiral can lower its energy by stretching the spin component along  $b$  direction and shrinking the spin component along  $c$  direction. The resulting spin state no longer has a simple form like Eq. (2). When the hard spin constraint is softened after fluctuations are included, the spin order may be approximated as an elliptical spin spiral. Such a magnetic order is actually observed in the  $\text{Fe}_{1+y}\text{Te}$  samples with  $y \gtrsim 0.12$ .<sup>17</sup> For the purpose of this section, we merely approximate the incommensurate ordered state as a circular spin spiral.

Now we consider the three candidate ground states: the bicollinear AFM state with spins aligned along  $b$  direction, the incommensurate state with a *circular* spin spiral in  $bc$  plane, and the Néel state with spins aligned along  $b$  direction. The classical energies of the three states are listed in Table I. Comparing these energies, we obtain a phase diagram depicted in Fig. 3. One should note that, because we approximate the incommensurate state as a circular spin spiral, the actual region for the incommensurate state should be larger than the one in Fig. 3. Moreover, from Table I, the  $J_{2b}$  exchange does not differentiate among the three states, whether it is small or large.

### C. Linear spin wave theory

Here we turn our attention to the spin-wave excitations that we study using the linear spin-wave analysis for the commensurate bicollinear and the incommensurate coplanar states that are experimentally relevant. For concreteness, we set  $D_a = D_b \equiv D$  in this subsection.

Since the commensurate bicollinear AFM state is not a proper state,<sup>21</sup> we label the two sublattices of the square

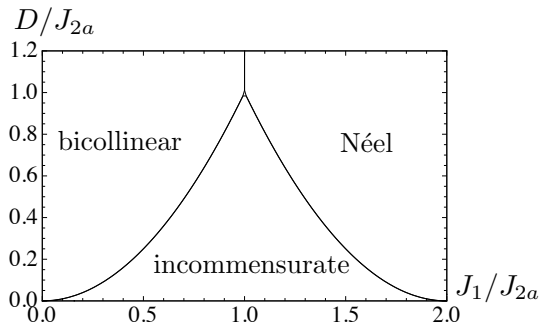


FIG. 3. The classical mean field phase diagram with  $D_a = D_b \equiv D$  and  $J_{2a} > 0$ .

lattice as A and B (see Fig. 2). The spin orientations are then parameterized as

$$\hat{n}_{A,i} = (-)^{(x_i - y_i)/2} \hat{b}, \quad (4a)$$

$$\hat{n}_{B,i} = (-)^{(x_i - y_i - 1)/2} \hat{b}, \quad (4b)$$

where  $x_i - y_i$  is even (odd) for A (B) sublattice. We set the lattice constants to unity.

The Holstein-Primakoff transformation for the spins is then given by

$$S_{\mu,i}^+ \equiv \mathbf{S}_{\mu,i} \cdot (\hat{c} + i\hat{n}_{\mu,i} \times \hat{c}) = \sqrt{2S} a_{\mu,i}, \quad (5a)$$

$$S_{\mu,i}^- \equiv \mathbf{S}_{\mu,i} \cdot (\hat{c} - i\hat{n}_{\mu,i} \times \hat{c}) = \sqrt{2S} a_{\mu,i}^\dagger, \quad (5b)$$

$$\mathbf{S}_{\mu,i} \cdot \hat{n}_{\mu,i} = S - a_{\mu,i}^\dagger a_{\mu,i}, \quad (5c)$$

where  $a_{\mu,i}^\dagger, a_{\mu,i}$  are bosonic creation and annihilation operators with  $\mu = A, B$  the sublattice index.

For the incommensurate state, it is difficult to parameterize the coplanar spin order that satisfies the hard spin constraint and optimizes the energy when the spin anisotropy is present. However, experimentally one finds that orthorhombic distortion is reduced and the incommensurate spin spiral becomes more circular as the Fe doping level is increased. Thus, to compute the spin-wave dispersion, we consider the Hamiltonian in the absence of the  $b$ -axis spin anisotropy and a circular spiral ground state in  $bc$  plane that applies to the regimes of high Fe dopings. The spin orientation is then given by

$$\hat{n}_i = \cos(k_1 x_i - k_1 y_i) \hat{b} + \sin(k_1 x_i - k_1 y_i) \hat{c}. \quad (6)$$

This is a proper spin state, and the spin operator can be parameterized as

$$S_i^+ \equiv \mathbf{S}_i \cdot (\hat{a} + i\hat{n}_i \times \hat{a}) = \sqrt{2S} a_i, \quad (7a)$$

$$S_i^- \equiv \mathbf{S}_i \cdot (\hat{a} - i\hat{n}_i \times \hat{a}) = \sqrt{2S} a_i^\dagger, \quad (7b)$$

$$\mathbf{S}_i \cdot \hat{n}_i = S - a_i^\dagger a_i. \quad (7c)$$

Plugging these two parameterization into the Hamiltonian Eq. (1) and keeping to quadratic order in the

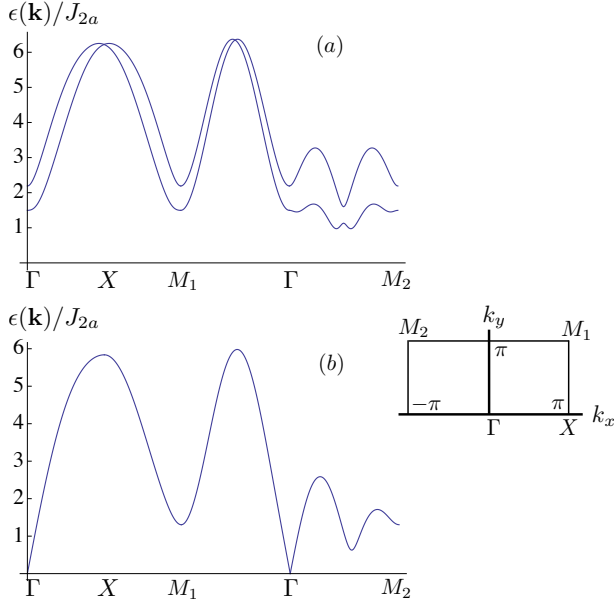


FIG. 4. The spin wave spectrum for (a) bicollinear state and (b) incommensurate coplanar spiral state. In (a),  $J_{2a} = J_{2b}$ ,  $J_1 = 0.4J_{2a}$ ,  $D = 0.2J_{2a}$ , with two dispersions corresponding to two spins within the magnetic unit cell. In (b),  $J_{2a} = J_{2b}$ ,  $J_1 = 0.4J_{2a}$ ,  $D = 0.05J_{2a}$ . The inset is part of the Brillouin zone with momentum points identified.

magnon operators, we obtain the linear spin-wave Hamiltonians. For the incommensurate spin spiral state,

$$H_{\text{IC}} = \sum_{\mathbf{k}} \epsilon_{\mathbf{k}}^{\text{IC}} a_{\mathbf{k}}^{\dagger} a_{\mathbf{k}} + \nu_{\mathbf{k}} a_{\mathbf{k}}^{\dagger} a_{-\mathbf{k}}^{\dagger} + \nu_{\mathbf{k}} a_{\mathbf{k}} a_{-\mathbf{k}} + \mathcal{N} E_{\text{IC}}(k_1, -k_1), \quad (8)$$

with  $\mathcal{N}$  the number of lattice sites,  $E_{\text{IC}}$  the ground state energy of the incommensurate state from Table I and

$$\epsilon_{\mathbf{k}}^{\text{IC}} = J_{2a} S [(1 + \cos 2k_1) \cos(k_x - k_y) - 2 \cos 2k_1] + 2J_{2b} S [1 - \cos(k_x + k_y)] + J_1 S [-4 \cos k_1 + (1 + \cos k_1)(\cos k_x + \cos k_y)] + DS, \quad (9a)$$

$$\nu_{\mathbf{k}} = \frac{1}{2} J_{2a} S (\cos 2k_1 - 1) \cos(k_x - k_y) - \frac{1}{2} DS + \frac{1}{2} J_1 S (\cos k_1 - 1) (\cos k_x + \cos k_y). \quad (9b)$$

In above expressions  $k_1$  is given by Eq. (3) which optimizes the classical energy.

For the commensurate bicollinear AFM state, we instead find

$$H_C = \sum_{\mathbf{k}, \mu} \epsilon_{\mathbf{k}}^C a_{\mathbf{k}\mu}^{\dagger} a_{\mathbf{k}\mu} + \sum_{\mathbf{k}} (\mu_{\mathbf{k}} a_{\mathbf{k}A}^{\dagger} a_{\mathbf{k}B} + m_{\mathbf{k}} a_{\mathbf{k}A}^{\dagger} a_{-\mathbf{k}B}^{\dagger} + n_{\mathbf{k}} a_{\mathbf{k}A}^{\dagger} a_{-\mathbf{k}A}^{\dagger} + n_{\mathbf{k}} a_{\mathbf{k}B}^{\dagger} a_{-\mathbf{k}B}^{\dagger} + h.c.) + \mathcal{N} E_C\left(\frac{\pi}{2}, -\frac{\pi}{2}\right) \quad (10)$$

with

$$\epsilon_{\mathbf{k}}^C = 2J_{2a} S + 2J_{2b} S [1 - \cos(k_x + k_y)] + 3DS, \quad (11a)$$

$$\mu_{\mathbf{k}} = m_{\mathbf{k}}^* = J_1 S (e^{ik_x} + e^{-ik_y}), \quad (11b)$$

$$n_{\mathbf{k}} = J_{2a} S \cos(k_x - k_y) - \frac{1}{2} DS. \quad (11c)$$

The corresponding spin-wave dispersions are straightforwardly obtained, and are depicted along the high symmetry lines in Fig. 4. We observe that the spin-wave excitation is gapped for the bicollinear AFM state as the spin-rotation symmetry is broken completely by the single-ion spin anisotropy. As expected on general symmetry grounds, for the incommensurate state we find a gapless spin-wave excitation spectrum. Because of the incommensurate nature of the state, it does not cost any energy to uniformly rotate all the spins about the  $a$ -axis and the spectrum remains gapless even if above analysis is extended to include lattice anisotropy.

#### D. Effective continuum model

The microscopic lattice model in Eq.(1) gives the ground states and spin excitation spectrum of  $\text{Fe}_{1+y}\text{Te}$  consistent with its experimental studies.<sup>15-18</sup> To study the low-energy fluctuations more universally and in more detail, particularly near continuous phase transitions and beyond mean-field theory, it is convenient to formulate the system's description using a continuum Landau-Wilson functional. The latter can be derived from the above microscopic model using a standard analysis of tracing over the microscopic spin degrees of freedom in the presence of finite local magnetization  $\langle \mathbf{S}_i \rangle \sim \phi_i$ . For a time-independent field configuration (sufficient for our purposes here), the harmonic Landau free energy functional is given by,

$$\mathcal{F}[\phi] = \frac{1}{2} \sum_{\mathbf{q}} \epsilon_{\mathbf{q}} |\phi_{\mathbf{q}}|^2 + \sum_{\mathbf{R}_i} (\tau_a |\phi_i^a|^2 + \tau_b |\phi_i^b|^2 + \tau_c |\phi_i^c|^2), \quad (12)$$

where the exchange induced dispersion is well-approximated by

$$\epsilon_{\mathbf{q}} = \frac{c_a}{4q_1^2} (q_a^2 - q_1^2)^2 + c_b q_b^2 \quad (13)$$

with a minimum at the incommensurate wavevector,  $q_1 = 2\pi - 2k_1$  and  $c_{a,b}, \tau_{a,b,c}$  functions of the microscopic parameters appearing in Hamiltonian (1) and of temperature,  $T$ . Moreover, the  $\tau_{a,b,c}$  terms arise from the easy  $ab$ -plane (transverse to  $c$ -axis) anisotropy together with the single-ion orthorhombic anisotropy. The experimental orthorhombic lattice phenomenology is encoded in the  $\tau_b < \tau_c < \tau_a$  ordering of these couplings, with the largest  $\tau_a$  confining the spin in the anisotropic  $bc$ -plane. The vanishing of  $\tau_b$  controls the continuous transitions from the orthorhombic paramagnet ( $\text{PM}_O$ ) to the bicollinear

AFM state. In Eq. (12) we have also changed the basis from the  $xy$  to  $ab$  coordinates (see Fig. 2) using

$$\begin{pmatrix} q_a \\ q_b \end{pmatrix} = R \begin{pmatrix} q_x \\ q_y \end{pmatrix}, \quad \begin{pmatrix} x_a \\ x_b \end{pmatrix} = \frac{1}{2} R \begin{pmatrix} x \\ y \end{pmatrix} \quad (14)$$

with

$$R = \begin{pmatrix} 1 & -1 \\ 1 & 1 \end{pmatrix}. \quad (15)$$

Now the lattice constants in  $ab$ -coordinates are defined as a full diagonal length of the lattice in  $xy$ -coordinates. In the following, we will work in the  $ab$  coordinates.

The free energy  $\mathcal{F}[\phi]$  captures the competition between the exchange and the anisotropy. The exchange dispersion,  $\epsilon_{\mathbf{q}}$ , (13) clearly favors an incommensurate ordering of spins at a wavevector  $(q_a, q_b) = (q_1, 0)$ , independent of the actual spin orientation, while the “ $\tau$ ” anisotropy terms favors a collinear state with magnetization ordered along  $b$ .

We note that to capture the spin-lattice commensuration effects above we were careful to keep the lattice sums in the “ $\tau$ ” lattice anisotropy terms. To go to a complete continuum limit, we coarse-grain these terms utilizing the Poisson summation formula

$$\frac{1}{v} \sum_{\mathbf{G}_n} e^{i\mathbf{G}_n \cdot \mathbf{r}} = \sum_{\mathbf{R}_i} \delta^d(\mathbf{r} - \mathbf{R}_i), \quad (16)$$

where  $\mathbf{G}_n$  is a reciprocal lattice vector,  $\mathbf{R}_i$  is the real-space lattice vector with  $v$  the volume of the primitive unit cell. Applying this to the single-ion anisotropy, we find that the continuum limit of this free energy is well-approximated by

$$\begin{aligned} \mathcal{F}_{\text{ani}}[\phi] &= \frac{1}{v} \sum_n \int_{\mathbf{r}} \sum_{\mu=a,b,c} \tau_{\mu} \phi^{\mu}(\mathbf{r})^2 e^{i2\pi n x_a} \\ &\approx \frac{1}{v} \int_{\mathbf{r}} \sum_{\mu=a,b,c} \tau_{\mu} \phi^{\mu}(\mathbf{r})^2 [1 + 2 \cos(2q_0 x_a)], \quad (17) \end{aligned}$$

with  $q_0 = \pi$  and the cosine encoding the underlying lattice discreteness along  $a$ -axis. Since we expect magnetic states that are periodic only along the  $a$ -axis, in going to the continuum limit we were safe to neglect the discreteness along other axes. We further note that we only kept the lowest reciprocal lattice harmonic, with higher ones weaker and far from the incommensurate wavevector  $q_1$ .

### E. Magnetoelastic coupling for the single-ion anisotropy

A semi-microscopic origin of single-ion spin anisotropy discussed above can be attributed to the structural orthorhombic lattice distortion that induces spin-anisotropy through spin-orbit interaction. To this end we

consider a general two-dimensional elastic energy density (here up to quadratic order in the strain) with a tetragonal symmetry

$$\mathcal{H}_{\text{el}}^0 = \frac{1}{2} [K_{11}(u_{xx}^2 + u_{yy}^2) + K_{12}u_{xx}u_{yy} + 2K_{44}u_{xy}^2] \quad (18)$$

where  $K_{11}$ ,  $K_{12}$ ,  $K_{44}$  are bulk and shear moduli and  $u_{\sigma\sigma'}$  is the elastic strain tensor. Anticipating the proximity to the tetragonal-to-orthorhombic structural transition, with principle axes  $a$  and  $b$  it is convenient to express  $\mathcal{H}_{\text{el}}$  in terms of the  $ab$  coordinates. The transformed strain tensor is then given by

$$U^{ab} = \begin{pmatrix} u_{aa} & u_{ab} \\ u_{ab} & u_{bb} \end{pmatrix} = R U^{xy} R^{-1} = R \begin{pmatrix} u_{xx} & u_{xy} \\ u_{xy} & u_{yy} \end{pmatrix} R^{-1} \quad (19)$$

with

$$u_{xx} = \frac{1}{2}(u_{aa} + u_{bb} + 2u_{ab}) \quad (20a)$$

$$u_{yy} = \frac{1}{2}(u_{aa} + u_{bb} - 2u_{ab}) \quad (20b)$$

$$u_{xy} = \frac{1}{2}(-u_{aa} + u_{bb}). \quad (20c)$$

Using these relations inside Eq. (18) gives

$$\begin{aligned} \mathcal{H}_{\text{el}}^0 &= \frac{1}{2} \left[ \left( \frac{1}{2}K_{11} + \frac{1}{4}K_{12} + \frac{1}{2}K_{44} \right) (u_{aa}^2 + u_{bb}^2) \right. \\ &\quad \left. + (K_{11} + \frac{1}{2}K_{12} - K_{44})u_{aa}u_{bb} + (2K_{11} - K_{12})u_{ab}^2 \right] \\ &\equiv \frac{1}{2} [K'_{11}(u_{aa}^2 + u_{bb}^2) + K'_{12}u_{aa}u_{bb} + K'_{44}u_{ab}^2] \quad (21) \end{aligned}$$

with transformed bulk and shear modulus  $K'_{11}$ ,  $K'_{12}$ , and  $K'_{44}$ . For the tetragonal to orthorhombic transition  $u_{xy} \neq 0$  and  $u_{xx} = u_{yy} = 0$ . Equivalently, in the  $ab$  coordinate system  $u_{aa} = -u_{bb} = u_0$  and  $u_{ab} = 0$ , reducing the elastic energy to

$$\mathcal{H}_{\text{el}}^0 = (K'_{11} - \frac{1}{2}K'_{12})u_0^2 \equiv K_{44}u_0^2 \quad (22)$$

In the presence of the orthorhombic distortion, the magneto-elastic coupling is given by

$$\begin{aligned} \mathcal{H}_{\text{me}} &= \alpha S^{\mu} U_{\mu\nu} S^{\nu} + g_{12} u_{xy}^2 \mathbf{S}^2 \\ &= \alpha u_{aa} (S^a)^2 + \alpha u_{bb} (S^b)^2 + g_{12} u_{xy}^2 \mathbf{S}^2. \quad (23) \end{aligned}$$

Then, including elastic nonlinearities for the orthorhombic strain  $u_0$ , the full magneto-elastic Hamiltonian in  $ab$  coordinates is given by,

$$\mathcal{H}_{\text{el}} = K_{44}u_0^2 + \frac{\lambda}{4}u_0^4 + \alpha u_0 [(S^a)^2 - (S^b)^2] + g_{12}u_0^2 \mathbf{S}^2, \quad (24)$$

which, after a structural transition to the orthorhombic state (characterized by  $u_0 > 0$ ) leads to the single-ion

anisotropy of the previous section, with  $D_a = D_b = \alpha u_0$ . Due to the planar geometry of FeTe, a  $c$ -axis spin anisotropy is also allowed by symmetry, both in the tetragonal and orthorhombic phases, and in the latter state generically leads to  $u_{aa} \neq -u_{bb}$  and therefore  $D_a \neq D_b$ .

In the above, we demonstrated that an orthorhombic lattice distortion induces the single-ion spin anisotropy through the magnetoelastic coupling. More generally, the spin anisotropy, lattice distortion, and the orbital degrees of freedom should all couple together. In particular, a Jahn-Teller mechanism is suggested to lift the orbital degeneracy and induce the lattice distortion. Such a Jahn-Teller effect can thus also generate the single-ion spin anisotropy.

### III. MAGNETOSTRUCTURAL TRANSITION

We now turn to a mean-field analysis of the magnetostructural transition of FeTe based on the above Landau theory, similar to Paul *et al.*<sup>22</sup>

In Fe<sub>1+y</sub>Te, the structural transition from tetragonal to orthorhombic (for high doping) or monoclinic (for low doping) is accompanied by the magnetic transition and as a result is naturally first order. However, in other iron pnictides the structural transition is observed to precede the magnetic transition. As we demonstrate below, our model captures both possibilities depending on the value of Landau parameters.

We begin with the Ginzburg-Landau free energy density,  $\mathcal{F}_{\text{GL}}$ ,

$$\mathcal{F}_{\text{GL}} = \mathcal{F}_{\text{M}} + \mathcal{F}_{\text{E}} + \mathcal{F}_{\text{ME}}, \quad (25a)$$

$$\mathcal{F}_{\text{M}} = \phi \cdot \hat{\epsilon}_0 \cdot \phi + \tau |\phi|^2 + \frac{g}{2} |\phi|^4, \quad (25b)$$

$$\mathcal{F}_{\text{E}} = \frac{B}{2} u_{xy}^2 + \frac{\lambda}{4} u_{xy}^4, \quad (25c)$$

$$\mathcal{F}_{\text{ME}} = \alpha [(\phi^a)^2 - (\phi^b)^2] u_{xy} + g_{12} |\phi|^2 u_{xy}^2, \quad (25d)$$

with all phenomenological couplings positive except  $\tau$  and  $B$  which can change sign at the structural and magnetic transitions.

As derived in the microscopic analysis of the lattice model the dispersion exhibits a minimum at a finite momentum  $q_1$  along the  $a$ -axis and in a continuum is well approximated by

$$\hat{\epsilon}_0 = \frac{c_a}{4q_1^2} (-\partial_a^2 - q_1^2)^2 - c_b \partial_b^2 - c_c \partial_c^2. \quad (26)$$

Thus we parameterize the magnetic order by a spiral in the  $b$ - $c$  plane

$$\phi(\mathbf{r}) = \text{Re}[(\psi^b(\mathbf{r})\hat{b} - i\psi^c(\mathbf{r})\hat{c})e^{iq_1 x_a}], \quad (27)$$

where  $\psi^\mu(\mathbf{r})$  is a local complex spiral order parameter, and, anticipating the  $b$ - $c$  coplanar and  $b$  bicollinear AFM states, we have taken  $\phi^a = 0$ . Because the magnetoelastic coupling in the  $a$ - $b$  plane for  $u_{xy} > 0$  lowers the

effective critical temperature for the  $\psi^b$  component (compared to  $\psi^c$ ), generically we expect the magneto-elastic transition to be well-characterized by a single magnetic component  $\phi \equiv \psi^b$ .

With this complex scalar parameterization, within a mean-field treatment the saddle point equations are given by

$$0 = \frac{\partial \mathcal{F}_{\text{GL}}}{\partial \phi^*} = \tau \phi + g |\phi|^2 \phi - \alpha \phi u_{xy} + g_{12} \phi u_{xy}^2 \quad (28a)$$

$$0 = \frac{\partial \mathcal{F}_{\text{GL}}}{\partial u_{xy}} = B u_{xy} - \frac{\alpha}{2} |\phi|^2 + g_{12} |\phi|^2 u_{xy} + \lambda u_{xy}^3. \quad (28b)$$

Firstly we observe that this general magnetoelastic coupling requires that a nonzero magnetic order always induces a structural distortions as it is coupled linearly to it. Thus, a tetragonal phase with magnetic order is in principle not allowed, though in any particular system the orthorhombic distortion can be quite small. Therefore, this model generically admits the following three phases:

1. Tetragonal paramagnet, PM<sub>T</sub> :  $\phi = 0, u_{xy} = 0,$
2. Orthorhombic paramagnet, PM<sub>O</sub> :  $\phi = 0$  and  $u_{xy} \neq 0,$
3. Orthorhombic commensurate or incommensurate AFM states, AFM<sub>O</sub> :  $\phi \neq 0$  and  $u_{xy} \neq 0$

We now map out the corresponding phase diagram. The PM<sub>T</sub> state occupies  $B > 0, \tau > 0$  part of the phase diagram.

For  $B < 0$  and  $\tau > 0$ , the system enters PM<sub>O</sub> state, characterized by order parameters,

$$\phi = 0 \quad (29a)$$

$$u_{xy} = \left(-\frac{B}{\lambda}\right)^{\frac{1}{2}}. \quad (29b)$$

The PM<sub>T</sub>-PM<sub>O</sub> phase boundary is therefore given by  $B = 0$  and  $\tau > 0$ .

On the other hand, for large  $B > 0, u_{xy} = 0$  is a minimum of  $\mathcal{F}_{\text{E}}$ , giving  $\tau = 0$  as the PM<sub>T</sub>-AFM<sub>O</sub> phase boundary at large positive  $B$ .

To determine the phase boundaries for smaller  $B > 0$ , we eliminate (or equivalently integrate out) the strain  $u_{xy}$  in favor of  $\phi$ , via

$$u_{xy} \simeq \frac{\alpha}{2B} |\phi|^2 \quad (30)$$

thereby obtaining an effective Landau free energy density inside PM<sub>T</sub>

$$\mathcal{F}_{\text{PM}_T} \simeq \frac{1}{2} \tau |\phi|^2 + \frac{1}{4} \left(g - \frac{\alpha^2}{2B}\right) |\phi|^4 + \frac{g_6}{6} |\phi|^6 + \dots \quad (31)$$

where  $g_6 = \frac{3\alpha^2 g_{12}}{4B^2}$ , and we neglected subdominant terms. For sufficiently large positive  $B$  (such that the  $g > \alpha^2/B$ ) the PM<sub>T</sub>-AFM<sub>O</sub> transition remains continuous at  $\tau = 0$ .



However, for  $B < B_c(\tau = 0) = \alpha^2/(2g)$  such that the quartic coupling turns negative, the transition is first-order at  $\tau_c(B)$  determined by

$$\mathcal{F}_{\text{PM}_T}(\phi_0) = 0 \quad (32a)$$

$$\left. \frac{\partial \mathcal{F}_{\text{PM}_T}}{\partial \phi^*} \right|_{\phi=\phi_0} = 0 \quad (32b)$$

These give

$$|\phi_0|^2 = \frac{-4\tau_c}{g - \frac{\alpha^2}{B}} \quad (33)$$

and a first-order transition boundary

$$\tau_c(B) = \frac{1}{16g_{12}} \left( \alpha - \frac{2gB}{\alpha} \right)^2, \quad \text{for } B > 0. \quad (34)$$

Although this analysis is quantitatively only valid for sufficiently large  $B > 0$ , such that elastic nonlinearities remain small, the qualitative behaviour (upturn in the  $\tau_c(B)$  boundary and the first-order nature of the transition) persists, as illustrated in Fig. 5.

In contrast, for  $B < 0$  regime,  $u_{xy}$  spontaneously develops a nonzero expectation value,  $u_0$ . For large negative  $B$ ,  $u_0$  is determined by balance of  $u_{xy}^2$  and  $u_{xy}^4$  terms while other terms are small in comparisons. This gives

$$u_0 \simeq \left( -\frac{B}{\lambda} \right)^{\frac{1}{2}} \quad (35)$$

as before and phase boundary is given by (from the saddle point equation),

$$\tau_c(B) = \alpha \left( -\frac{B}{\lambda} \right)^{\frac{1}{2}} - \frac{g_{12}B}{\lambda}, \quad \text{for (large) } B < 0 \quad (36)$$

However for small negative  $B$ , the term linear in  $u_{xy}$  dominates over the  $Bu_{xy}^2$  term. Therefore  $u_0 \simeq (\frac{\alpha}{2\lambda}|\phi|^2)^{1/3}$  and the effective free energy density is given by

$$\begin{aligned} \mathcal{F}_{\text{PM}_O} \simeq & \frac{1}{2}\tau|\phi|^2 + \frac{1}{4}g|\phi|^4 + \frac{B}{2} \left( \frac{\alpha}{2\lambda} \right)^{\frac{2}{3}} |\phi|^{\frac{4}{3}} \\ & - \frac{3\lambda}{4} \left( \frac{\alpha}{2\lambda} \right)^{\frac{4}{3}} |\phi|^{\frac{8}{3}}. \end{aligned} \quad (37)$$

From this form, we find a first-order transition. Combining the components analysis, we obtain the phase diagram in Fig. 5.

For low Fe doping experiments of  $\text{Fe}_{1+y}\text{Te}$ <sup>5,6,17</sup> suggest that the reducing temperature takes the system across the first-order phase boundary in the positive  $\tau$ - $B$  quadrant of phase diagram in Fig. 5. This leads to a simultaneous orthorhombic distortion and development of bicollinear AFM order. In contrast, FeAs compounds which exhibit distinct continuous structural and magnetic transitions, are accommodated by a temperature path through a continuous phase boundary illustrated in the phase diagram.

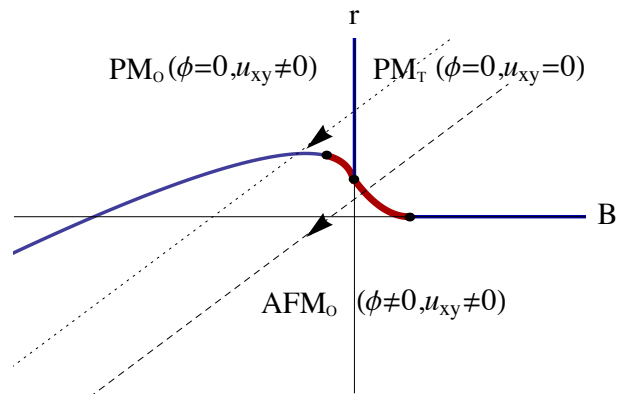


FIG. 5. (Color online) The global phase diagram in the reduced exchange,  $\tau$  and bulk modulus  $B$  plane. For low Fe doping, experiments<sup>5,6,17</sup> suggest that the reducing temperature follows the dashed curve taking the system across the first-order phase boundary (red thick curve) in the positive  $\tau$ - $B$  quadrant, that leads to a simultaneous orthorhombic distortion and development of bicollinear AFM order. The blue phase boundaries indicate second-order phase transitions, and in FeAs materials are crossed via two distinct, structural and magnetic transitions, as indicated by the dotted curve.

#### IV. BICOLLINEAR-TO-SPIRAL LOW-TEMPERATURE TRANSITION

Focusing on low-temperatures we now examine the nature of transition between the commensurate bicollinear state and the incommensurate planar spiral state, that is observed to take place in  $\text{Fe}_{1+y}\text{Te}$  at low temperatures, around the doping level  $y \simeq 0.12$ .<sup>17</sup> The transition is driven by a competition between the exchange energy that prefers a generically incommensurate spiral order at  $q_1$  and a single-ion spin anisotropy that selects a commensurate bicollinear AFM state at a wavevector  $q_0$ . As mentioned earlier, the orthorhombic distortion is observed to be reduced with increasing Fe doping. We therefore expect the single-ion spin anisotropy to also be reduced with the increased doping level, leading to a commensurate-incommensurate (CI) transition when the spin anisotropy energy drops below the exchange interaction. We analyze this competition and the resulting CI transition by starting with the Landau-Wilson free energy functional

$$\begin{aligned} \mathcal{F}[\phi] \approx & \frac{1}{2} \sum_{\mathbf{q}} \epsilon_{\mathbf{q}} |\phi_{\mathbf{q}}|^2 + \frac{1}{v} \int_{\mathbf{r}} [\tau_a |\phi^a|^2 + \tau_b |\phi^b|^2 + \tau_c |\phi^c|^2] \\ & \times [1 + 2 \cos(2q_0 x_a)], \end{aligned} \quad (38)$$

for the orthorhombic state,  $\tau_b < \tau_c < \tau_a$  derived above.



### A. Commensurate-incommensurate transition

In the bicollinear AFM state, we parameterize the coarse-grained magnetic order as

$$\phi(\mathbf{r}) = \psi_0 \cos[q_0 x_a - \theta(\mathbf{r})] \hat{b}, \quad (39)$$

with the magnetic wavevector  $q_0 = \pi$ . This parameterization neglects the subdominant “massive” spin fluctuations away from the easy  $b$ -axis, focusing on the phase variable  $\theta(\mathbf{r})$ . The free energy density, Eq. (38) then reduces to a standard Pokrovsky-Talapov form<sup>23</sup>

$$f[\theta] = \frac{\kappa}{2} (\partial_{x_a} \theta)^2 - \kappa Q \partial_{x_a} \theta - \sigma \cos(2\theta) \quad (40)$$

where  $\kappa = c_a \psi_0^2 / 2$ ,  $\sigma = -\tau_b \psi_0^2 / 2v$  and  $Q = q_0 - q_1$ , with  $Q \ll q_0$ , as is the case in experiments.<sup>17,18</sup> In above we dropped  $\theta$ -independent terms and neglected spatial dependence transverse to the  $a$ -axis.

The analysis of this Pokrovsky-Talapov free energy is quite standard.<sup>23</sup> We thus omit all technical details, focussing instead on the qualitative description and results necessary for our calculation of the structure factor near the CI transition.

Deep in the bicollinear AFM state, the single-ion anisotropy,  $\cos(2\theta)$  locks the phase field  $\theta(x_a)$  to zero, thereby leading to spin order commensurate with the lattice. In this state the exchange energy is frustrated because the bicollinear AFM order at  $q_0$  is not at the minimum  $q_1$  of the exchange dispersion. This is captured by the linear gradient term,  $-Q \partial_{x_a} \theta$  that (when balanced against the exchange  $(\partial_{x_a} \theta)^2$ ) seeks to induce a constant gradient  $Q$  in  $\theta$ , thereby shifting magnetic order down to  $q_1$ . With increasing iron doping, we expect the exchange energy to dominate over the single-ion spin anisotropy and thereby to drive the system through the commensurate-incommensurate transition at  $Q_c$  from the commensurate bicollinear AFM order at  $q_0$  to an incommensurate coplanar spiral order at  $q_1$ , with

$$Q_c = \frac{4}{\pi} \sqrt{\frac{\sigma}{\kappa}}. \quad (41)$$

The CI transition critical point is defined by the condition that the energy of a single domain wall in the commensurate state (a spin “soliton”) vanishes at  $Q_c$ .<sup>23</sup>

At low temperatures, we can ignore thermal fluctuations and approximate  $c_a \approx J_{2a}$ ,  $Q \approx J_1 / J_{2a}$  and  $\tau_b \approx -D_b$ , leading to  $Q_c \approx (4/\pi)(D_b / J_{2a})^{1/2}$ . The system then develops an incommensurate spin state for

$$D_b \lesssim \frac{\pi^2 J_1^2}{16 J_{2a}} \equiv D_b^{CI}. \quad (42)$$

For  $Q > Q_c$ , the system enters the incommensurate state. At low temperature, inside the magnetically ordered orthorhombic state this is captured in terms of a proliferation of  $\pi$ -solitons in  $\theta(x_a)$ , that thereby transitions from its zero value in the bicollinear AFM state to

a periodic array of  $\pi$ -solitons. Simple dimensional analysis dictates that a soliton is characterized by a width  $\xi = \sqrt{\sigma/\kappa}$  across which the phase  $\theta(x_a)$  advances by  $\pi$ . For a soliton spacing  $d(Q)$ , on average this induces a linear tilt of  $\theta$  with  $x_a$ ,

$$\langle \partial_{x_a} \theta \rangle \equiv \delta q(Q) \approx \pi/d, \quad (43)$$

that corresponds to a shift in the average spin density-wave wavevector  $q(Q) = q_0 - \delta q(Q)$  from  $q_0$  down to  $q_1$ . The soliton density  $\delta q(Q)$  grows with  $Q$  from 0, asymptotically approaching  $q_0 - q_1$  deep in the incommensurate state. At finite temperature its monotonically increasing functional form exhibits three regimes of  $Q$ .<sup>23</sup>

Because generically a  $c$ -component of  $\phi$  is nonzero inside the coplanar incommensurate spiral phase, our above parameterization of  $\phi(\mathbf{r})$ , (39) is technically incomplete. It thereby describes a CI transition from the commensurate bicollinear AFM state to incommensurate *collinear* (rather than coplanar) state. At low temperatures we expect the hard spin constraint to play an important role, and drive the system to develop a  $c$ -component of  $\phi$ . Thus, the transition is to an elliptical incommensurate planar spiral state. However, because close to the CI transition the coplanar incommensurate regions and the associated phase slips are confined inside solitons (that are dilute), we expect this approximation of neglecting  $c$ -component of  $\phi$  to be adequate. Namely, we expect that near CI the full solution is characterized by a highly eccentric elliptical polarization with  $\phi^c \ll \phi^b$ , which is observed in experiments.<sup>17</sup>

### B. Static spin structure factor near the commensurate-incommensurate transition

We now use above analysis of the commensurate-incommensurate transition to compute the static spin structure factor,

$$S(\mathbf{q}) \sim \int_{\mathbf{r}, \mathbf{r}'} e^{-i\mathbf{q} \cdot (\mathbf{r} - \mathbf{r}')} \langle \phi^b(\mathbf{r}) \phi^b(\mathbf{r}') \rangle. \quad (44)$$

To compute  $S(\mathbf{q})$  we use the parameterization Eq. (39), with  $\theta(x_a)$  inside the incommensurate state given by a soliton array,

$$\theta(x_a) = \delta q x_a + \delta \theta(x_a), \quad (45)$$

where the first term is the average phase from Eq.(43) and  $\delta \theta(x_a) \equiv \theta(x_a) - \delta q x_a$  is of a saw-tooth form, that can be well-approximated by a periodically-extended linear function

$$\delta \theta(x_a) = -\frac{\pi}{d} x_a, \quad \text{for } -d/2 < x \leq d/2, \quad (46)$$

as illustrated in Fig. 6.

We note that at large  $Q \gg Q_c$ ,  $\delta \theta$  vanishes,  $\delta q(Q) \rightarrow Q = q_0 - q_1$ , giving  $q_0 x_a - \theta(x_a) \approx q_1 x_a$  (see Eq.(39)).

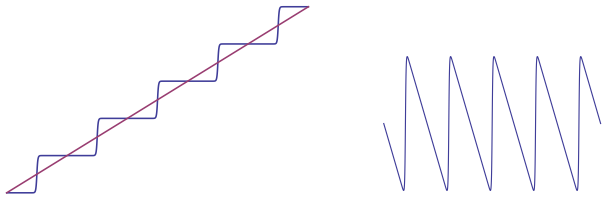


FIG. 6. Left:  $\theta(x)$  (Elliptic integral of the second kind) displaying a train of domain walls in the incommensurate state, just above  $Q_c$ , as well as the average tilted form  $\bar{\theta}(x) = qx$  (in red). Right: A train of domain walls in the incommensurate state,  $\delta\theta = \theta(x) - \bar{\theta}(x)$ , just above  $Q_c$ , after  $\bar{\theta}(x) = qx$  has been subtracted.

This reduces the ordering wave vector from the commensurate  $q_0$  to the incommensurate  $q_1$  wavevector. Thus, in this asymptotic limit the spin structure factor displays magnetic Bragg peaks at integer multiples of  $q_1$ .

For the intermediate values of  $Q > Q_c$  at zero temperature, the static structure factor is simply given by a Fourier transform that includes the soliton contribution,  $e^{i\delta\theta(x_a)}$ , that can be easily evaluated in the above linear (saw-tooth) approximation. Taking  $x_a = dn + x$ , we find

$$\begin{aligned}
 & S(q_a, q_b = 0) \\
 & \propto |\phi^b(q_a, q_b = 0)|^2 \\
 & \simeq \left| \sum_{n \in \mathcal{Z}} e^{-i(q_a - q_0 + \delta q)dn} \int_{-d/2}^{d/2} dx e^{-i(q_a - q_0 + \delta q - \pi/d)x} \right|^2 \\
 & \simeq \sum_{p \in \mathcal{Z}} \frac{1}{(2p - 1)^2} \delta(q_a - q_0 + \delta q - \frac{2\pi}{d}p) \quad (47)
 \end{aligned}$$

Thus, as anticipated, just above  $Q_c$  the appearance of solitons above the CI transition leads to a characteristic scattering consisting of a sequence of Bragg peaks at  $q_p = q_0 - \delta q + 2\pi p/d$ , with the amplitude  $A_p = 1/(2p - 1)^2$ .

At a finite temperature, fluctuations about  $\theta_s(x)$  need to be included. However, because these are described by an  $xy$ -model (since spatial rotational invariance is explicitly broken), we expect that in 3d these fluctuations are finite and lead to a nonvanishing Debye-Waller factor suppressing the amplitude of the Bragg peaks but leaving them sharp at the limit of the resolution (or with a finite width set by disorder). Generalization of this analysis to a dynamic structure function may be of interest in comparing with inelastic neutron scattering, but will not be performed here.

We next turn our attention to the static and dynamic structure factors near the finite temperature paramagnetic to magnetic transition, with the goal to understand the aforementioned neutron scattering phenomenology of the  $\text{Fe}_{1+y}\text{Te}$  observed by Parshall *et al.*<sup>18</sup>

## V. STATIC AND DYNAMIC SPIN STRUCTURE FACTORS NEAR THE MAGNETIC TRANSITION

We now study the spin hydrodynamics of  $\text{Fe}_{1+y}\text{Te}$  in the ordered ( $T < T_N$ ) and paramagnetic ( $T > T_N$ ) phases near the finite-temperature transition at  $T_N$  into the magnetic ordered states. Our motivation here is to understand the anomalous behavior of the dynamical spin structure factor of  $\text{Fe}_{1+y}\text{Te}$  recently observed by Parshall, *et al.* in the inelastic neutron scattering experiments near  $T_N$ .<sup>18</sup> Studying  $\text{Fe}_{1.08}\text{Te}$ , which exhibits a commensurate bicollinear AFM order and an associated Bragg peak at lower temperatures, they found that above  $T_N = 67.5\text{K}$ , the inelastic scattering is peaked at an incommensurate wavevector and zero frequency.<sup>18</sup> At the magnetic transition, this incommensurate diffuse peak precipitously shifts to a commensurate wavevector characteristic of the bicollinear AFM state. Furthermore, in this ordered state a spin wave excitation gap is observed, consistent with other experiments.<sup>15</sup>

With these experiments performed at a relatively high temperature regime, *i.e.* near  $T_N$ , we will utilize a classical hydrodynamic description, extending the planar magnet hydrodynamics<sup>19,20</sup> to spiral states with single ion anisotropy appropriate to  $\text{Fe}_{1+y}\text{Te}$ , finding qualitative agreement with experiments.<sup>18</sup>

### A. Static spin structure function in orthorhombic paramagnetic state

Before turning to the calculation of the dynamical spin structure factor, it is instructive to compute the static structure factor in the orthorhombic paramagnetic state ( $\text{PM}_O$ ) just above the transition to the bicollinear planar spiral state. We note that, although in  $\text{Fe}_{1+y}\text{Te}$  this  $\text{PM}_O$  phase has not been observed (as it undergoes a direct first-order transition from tetragonal paramagnet ( $\text{PM}_T$ ) to magnetically ordered orthorhombic phase), generically  $\text{PM}_O$  is allowed by symmetry and has been observed in other materials.<sup>24,25</sup> The static spin structure factor elucidates the competition between the incommensurate spiral state selected by the exchange interaction and the commensurate state imposed by the single-ion anisotropy.

To compute the static spin structure factor, we utilize the free energy in Eq. (12). Here, we reparameterize the magnetic order parameter as

$$\phi(\mathbf{r}) = \text{Re}[\psi(\mathbf{r})(\hat{b} - i\hat{c})e^{iq_1 x_a}], \quad (48)$$

where for simplicity we assumed circular polarization taking  $\psi^b(\mathbf{r}) = \psi^c(\mathbf{r}) \equiv \psi(\mathbf{r})$  as a local complex spiral order parameter and took  $\phi^a = 0$ . With this parameterization and in the continuum limit, the free energy in Eq. (12) reduces to

$$\mathcal{F} = \frac{1}{2} \sum_{\mathbf{k}} \tilde{\epsilon}_{\mathbf{k}} |\psi|^2 - \frac{1}{2} \int_{\mathbf{r}} D_{bc} \left( \psi^2 e^{2iQx_a} + c.c. \right) \quad (49)$$

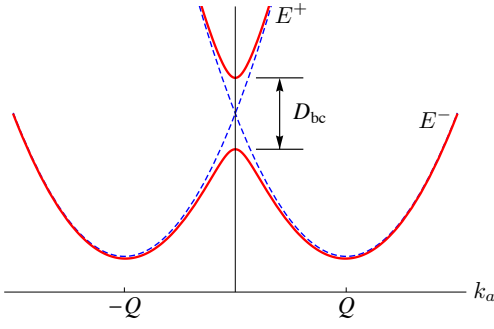


FIG. 7. The spectra showing two shifted parabolas (dashed curves) hybridized (most strongly at their crossings) in proportion to the single-ion anisotropy coupling  $D_{bc}$ .

with  $\mathbf{k} = \mathbf{q} - q_1 \hat{\mathbf{a}}$  measured relative to the incommensurate momentum  $q_1 \hat{\mathbf{a}}$  set by the spin dispersion minimum,  $\tilde{\epsilon}_{\mathbf{k}} = c_a k_a^2 + c_b k_b^2 + \tau$ ,  $\tau = \tau_b + \tau_c$ , and  $D_{bc} = \frac{1}{2v}(\tau_c - \tau_b)$ . Using  $\psi(\mathbf{r}) = \frac{1}{\sqrt{A}} \sum_{\mathbf{k}} \psi_{\mathbf{k}} e^{i\mathbf{k}\cdot\mathbf{r}}$ , standard diagonalization gives,

$$\mathcal{F} = \frac{1}{2} \sum_{\mathbf{k}} [E_{\mathbf{k}}^+ |\psi_{\mathbf{k}}^+|^2 + E_{\mathbf{k}}^- |\psi_{\mathbf{k}}^-|^2] \quad (50)$$

where

$$\begin{pmatrix} \psi_{\mathbf{k}+\mathbf{Q}} \\ \psi_{-\mathbf{k}+\mathbf{Q}}^* \end{pmatrix} = \begin{pmatrix} u_{\mathbf{k}} & -v_{\mathbf{k}}^* \\ v_{\mathbf{k}} & u_{\mathbf{k}}^* \end{pmatrix} \begin{pmatrix} \psi_{\mathbf{k}}^+ \\ \psi_{\mathbf{k}}^- \end{pmatrix} = \begin{pmatrix} u_{\mathbf{k}} \psi_{\mathbf{k}}^+ - v_{\mathbf{k}}^* \psi_{\mathbf{k}}^- \\ v_{\mathbf{k}} \psi_{\mathbf{k}}^+ + u_{\mathbf{k}}^* \psi_{\mathbf{k}}^- \end{pmatrix} \quad (51)$$

with  $\mathbf{Q} = Q\hat{\mathbf{a}}$ . The coefficients,  $u_{\mathbf{k}}$  and  $v_{\mathbf{k}}$ , are given by

$$u_{\mathbf{k}} = \frac{1}{\sqrt{2}} \left( 1 + \frac{\epsilon_{\mathbf{k}-}}{E_{\mathbf{k}}} \right)^{1/2}, \quad v_{\mathbf{k}} = \frac{1}{\sqrt{2}} \left( 1 - \frac{\epsilon_{\mathbf{k}-}}{E_{\mathbf{k}}} \right)^{1/2} \quad (52)$$

with

$$\epsilon_{\mathbf{k}\pm} = \frac{1}{4} (\tilde{\epsilon}_{\mathbf{k}+\mathbf{Q}} \pm \tilde{\epsilon}_{-\mathbf{k}+\mathbf{Q}}), \quad (53a)$$

$$E_{\mathbf{k}} = \sqrt{\epsilon_{\mathbf{k}-}^2 + D_{bc}^2}, \quad (53b)$$

$$E_{\mathbf{k}}^{\pm} = \epsilon_{\mathbf{k}\pm} \pm E_{\mathbf{k}}. \quad (53c)$$

The hybridization of the spectra via single-ion anisotropy is depicted in Fig. 7.

We express the magnetic order parameter  $\phi_{\mathbf{q}}^b$  in terms of these normal modes,

$$\phi_{\mathbf{q}}^b = \frac{1}{2} (v_{\mathbf{q}+\mathbf{q}_0}^* \psi_{\mathbf{q}+\mathbf{q}_0}^{+*} + u_{\mathbf{q}+\mathbf{q}_0} \psi_{\mathbf{q}+\mathbf{q}_0}^{-*} + u_{\mathbf{q}-\mathbf{q}_0}^* \psi_{\mathbf{q}-\mathbf{q}_0}^{+*} - v_{\mathbf{q}-\mathbf{q}_0} \psi_{\mathbf{q}-\mathbf{q}_0}^{-*}) \quad (54)$$

with  $\mathbf{q}_0 = q_0 \hat{\mathbf{a}}$ . Using equipartition for the correlation function of the normal modes in the paramagnetic state,

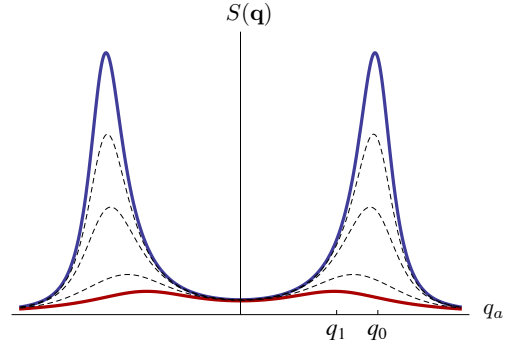


FIG. 8. The static structure factor  $S(\mathbf{q})$  in the  $\text{PM}_O$  state, where the shift of peaks from incommensurate wavevector  $q_1$  (bottom curve) to commensurate wavevector  $q_0$  (top curve) are shown. The dashed curves are for temperature intermediate values with the temperature increases from the top curve to bottom curve. The plot is displayed in arbitrary unit.

we obtain the static structure factor for  $T > T_N$ ,

$$\begin{aligned} S(\mathbf{q}) &\equiv \langle \phi_{\mathbf{q}}^{b*} \phi_{\mathbf{q}}^b \rangle \\ &= \frac{k_B T}{2} \left[ \frac{|v_{\mathbf{q}+\mathbf{q}_0}|^2}{E_{\mathbf{q}+\mathbf{q}_0}^+} + \frac{|u_{\mathbf{q}+\mathbf{q}_0}|^2}{E_{\mathbf{q}+\mathbf{q}_0}^-} + \frac{|u_{\mathbf{q}-\mathbf{q}_0}|^2}{E_{\mathbf{q}-\mathbf{q}_0}^+} + \frac{|v_{\mathbf{q}-\mathbf{q}_0}|^2}{E_{\mathbf{q}-\mathbf{q}_0}^-} \right] \\ &= \frac{k_B T}{8} \left[ \frac{\tilde{\epsilon}_{\mathbf{q}+\mathbf{q}_0+\mathbf{Q}}}{E_{\mathbf{q}+\mathbf{q}_0}^+ E_{\mathbf{q}+\mathbf{q}_0}^-} + \frac{\tilde{\epsilon}_{-\mathbf{q}+\mathbf{q}_0+\mathbf{Q}}}{E_{\mathbf{q}-\mathbf{q}_0}^+ E_{\mathbf{q}-\mathbf{q}_0}^-} \right]. \quad (55) \end{aligned}$$

The spin structure factor is displayed for varying reduced temperature  $\tau$  in the  $\text{PM}_O$  state in Fig. 8.

## B. Dynamic structure factor in paramagnetic state, $\text{PM}_O$

We now turn to the computation of the dynamic structure factor, first focusing on the paramagnetic state. Because the primary experiments<sup>18</sup> of our interest take place at a relatively high temperature near the thermal transition to the magnetic state, we utilize a classical hydrodynamic description.<sup>19</sup> Standard symmetry arguments, together with nontrivial spin commutation relations that encode precession lead to a model E hydrodynamics, described by coupled Langevin equations,

$$\partial_t \phi = -2\gamma \frac{\delta \mathcal{F}}{\delta \phi^*} - i\Gamma \phi \frac{\delta \mathcal{F}}{\delta m} + \zeta \quad (56a)$$

$$\partial_t m = \lambda \nabla^2 \frac{\delta \mathcal{F}}{\delta m} + 2\Gamma \text{Im} \left( \phi^* \frac{\delta \mathcal{F}}{\delta \phi^*} \right) + \zeta_m \quad (56b)$$

where  $\mathcal{F}$  is from Eq.(38),  $\phi = \phi^b + i\phi^c$ ,  $m = \phi^a$  are local transverse and longitudinal magnetization components, and  $\Gamma, \gamma, \lambda$  are hydrodynamic coefficients characterizing the system.  $\zeta = \zeta_b + i\zeta_c$ ,  $\zeta_m$  are components of the thermal Gaussian noise characterized by a vanishing mean,  $\langle \zeta_\sigma \rangle = \langle \zeta_m \rangle = 0$  and variances imposed by the

fluctuation-dissipation relation,<sup>19</sup>

$$\langle \zeta_\sigma(\mathbf{r}, t) \zeta_{\sigma'}(\mathbf{r}', t') \rangle = 2\gamma k_B T \delta_{\sigma\sigma'} \delta(\mathbf{r} - \mathbf{r}') \delta(t - t') \quad (57a)$$

$$\langle \zeta_m(\mathbf{r}, t) \zeta_m(\mathbf{r}', t') \rangle = -2\lambda k_B T \nabla^2 \delta(\mathbf{r} - \mathbf{r}') \delta(t - t'), \quad (57b)$$

with  $\sigma = b, c$ . The equations consist of dissipative (relaxational) terms as well as the reactive parts that capture the spin precessional dynamics, as studied extensively for numerous other magnetic systems. The new ingredient here is the spiral nature of the ordered state and the single-ion pinning anisotropy special to  $\text{Fe}_{1+y}\text{Te}$ .

In the disordered paramagnetic state, it is sufficient to work within the harmonic approximation, where the nonlinear precessional terms can be neglected. Thus, the equations of motion considerably simplify to the model B form.<sup>19</sup> The equation for the longitudinal magnetization  $m$  decouples giving a simple diffusive mode for the spin  $a$  component. We focus on the transverse modes encoded in the complex order parameter  $\phi$ , that satisfies

$$\partial_t \phi = -\gamma [(\hat{\epsilon}_0 + \tau)\phi - 4D_{bc}\phi^* \cos(2q_0 x_a)] + \zeta. \quad (58)$$

---


$$\begin{aligned} S(\mathbf{q}, \omega) &\equiv \langle \phi^b(\mathbf{q}, \omega) \phi^b(-\mathbf{q}, -\omega) \rangle \\ &= \frac{1}{4} \langle \psi(\mathbf{q} - \mathbf{q}_1, \omega) \psi^*(\mathbf{q} - \mathbf{q}_1, \omega) \rangle + \frac{1}{4} \langle \psi^*(-\mathbf{q} - \mathbf{q}_1, -\omega) \psi(-\mathbf{q} - \mathbf{q}_1, -\omega) \rangle \\ &= \frac{\gamma k_B T [\omega^2 + \gamma^2 (\tilde{\epsilon}_{\mathbf{q}+\mathbf{q}_0+\mathbf{Q}}^2 + 4D_{bc}^2)]}{[-\omega^2 + 4\gamma^2 (\epsilon_{\mathbf{q}+\mathbf{q}_0,+}^2 - E_{\mathbf{q}+\mathbf{q}_0}^2)]^2 + (4\gamma\omega\epsilon_{\mathbf{q}+\mathbf{q}_0,+})^2} + \frac{\gamma k_B T [\omega^2 + \gamma^2 (\tilde{\epsilon}_{-\mathbf{q}+\mathbf{q}_0+\mathbf{Q}}^2 + 4D_{bc}^2)]}{[-\omega^2 + 4\gamma^2 (\epsilon_{-\mathbf{q}+\mathbf{q}_0,+}^2 - E_{-\mathbf{q}+\mathbf{q}_0}^2)]^2 + (4\gamma\omega\epsilon_{-\mathbf{q}+\mathbf{q}_0,+})^2}. \end{aligned} \quad (63)$$

For a range of parameters,  $S(\mathbf{q}, \omega)$  is illustrated in Fig. 9. It displays an  $\omega = 0$  Lorentzian peak and a shift of its finite  $\mathbf{q}$  peaks from the incommensurate to commensurate values as observed in experiments by Parshall *et al.*<sup>18</sup> Consistent with the fluctuation-dissipation theorem, integration of  $S(\mathbf{q}, \omega)$  over  $\omega$  also gives the static structure factor obtained directly in Sec. IV A, Eq. (55) and illustrated in Fig. 8.

### C. Dynamic structure function in planar spiral state

#### 1. Incommensurate phase

Next we turn to the computation of the dynamic structure factor inside the *incommensurate* planar spiral state. Starting with the free energy, Eq. (38), and neglecting the  $bc$  plane spin-anisotropy (as it is averaged out in the

Using Eq. (48),  $\phi = \psi e^{iq_1 x_a}$  for the spin spiral state parameterization we obtain

$$\begin{aligned} \frac{\partial}{\partial t} \begin{pmatrix} \psi_{\mathbf{k}+\mathbf{Q}} \\ \psi_{-\mathbf{k}+\mathbf{Q}}^* \end{pmatrix} &= -\gamma \begin{pmatrix} \tilde{\epsilon}_{\mathbf{k}+\mathbf{Q}} & -2D_{bc} \\ -2D_{bc} & \tilde{\epsilon}_{-\mathbf{k}+\mathbf{Q}} \end{pmatrix} \begin{pmatrix} \psi_{\mathbf{k}+\mathbf{Q}} \\ \psi_{-\mathbf{k}+\mathbf{Q}}^* \end{pmatrix} \\ &\quad + \begin{pmatrix} \zeta_{\mathbf{k}+\mathbf{q}_0} \\ \zeta_{-\mathbf{k}+\mathbf{q}_0}^* \end{pmatrix} \end{aligned} \quad (59)$$

where  $\tilde{\epsilon}_{\mathbf{k}} = c_a k_a^2 + c_b k_b^2 + \tau$  and  $\zeta_{\mathbf{q}}$  is a spatial Fourier transform of  $\zeta(\mathbf{r})$  with

$$\langle \zeta_{\mathbf{k}}^*(t) \zeta_{\mathbf{k}}(t') \rangle = 4\gamma k_B T \delta(t - t'). \quad (60)$$

After Fourier transformation, we find

$$\psi(\mathbf{k} + \mathbf{Q}, \omega) = C_{\mathbf{k}} \left[ (i\omega + \gamma \tilde{\epsilon}_{-\mathbf{k}+\mathbf{Q}}) \zeta_{\mathbf{k}+\mathbf{q}_0} + 2\gamma D_{bc} \zeta_{-\mathbf{k}+\mathbf{q}_0} \right], \quad (61)$$

where

$$C_{\mathbf{k}} = [-\omega^2 + 4\gamma^2 (\epsilon_{\mathbf{k}+}^2 - E_{\mathbf{k}}^2 + i\omega\epsilon_{\mathbf{k}+}/\gamma)]^{-1}. \quad (62)$$

From we obtain the dynamic spin structure factor

---

incommensurate state), the free energy reduces to

$$\mathcal{F} = \frac{1}{2} \int dx_a dx_b \left[ \sum_{\mu=b,c} \phi^\mu \hat{\epsilon}_0 \phi^\mu + \chi_m^{-1} m^2 \right], \quad (64)$$

with  $\chi_m$  the  $a$ -axis magnetic susceptibility. To treat the dynamics we need to include the  $a$ -component of the magnetization,  $m$ , because it is a field conjugate to the hydrodynamic mode  $\phi = \phi^b + i\phi^c$  and therefore appears in the spin precessional term in the equations of motion. In the spiral state it appears even at a harmonic level. This contrasts with the statics (Sec. IV A, where  $m$  is “gapped” and therefore at low energies can be neglected) and with the disordered state dynamics (Sec. V B, where in the harmonic approximation  $m$  decouples from the transverse Goldstone modes,  $\phi^{b,c}$ ). The hydrodynamic equations for the complex  $\phi$  order parameter and its conjugate field  $m$  become

$$\partial_t \phi = -\gamma \hat{\epsilon}_0 \phi - i\Gamma \chi_m^{-1} m \phi + \zeta, \quad (65a)$$

$$\partial_t m = D_m \nabla^2 m + \Gamma \text{Im}(\phi^* \hat{\epsilon}_0 \phi) + \zeta_m, \quad (65b)$$

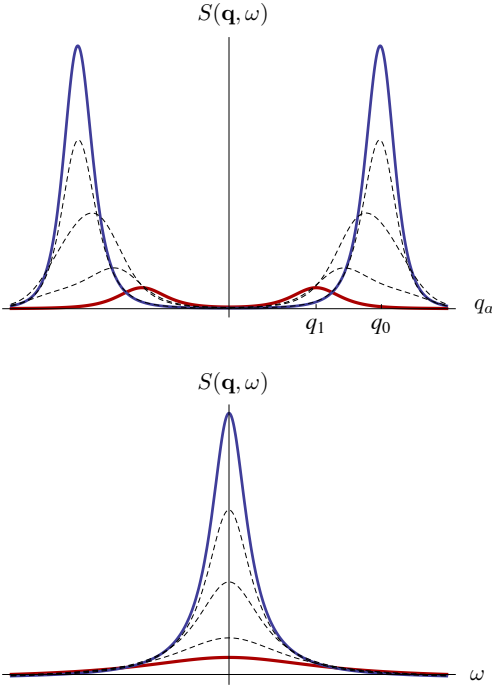


FIG. 9. The dynamic structure factors  $S(\mathbf{q}_a, \omega)$  from Eq.(63) as a function of  $q_a$  (top) and  $\omega$  (bottom). As the transition to the SDW at  $T_N$  is approached it exhibits a shifting and growth of the finite momentum peak from the incommensurate state at  $q_1$  (red) at high temperature toward the commensurate value  $q_0$  (top). The dashed lines are the value for intermediate temperatures. The Lorentzian peak at  $\omega = 0$  represents the relaxational dynamics characteristic of the paramagnetic phase.

with  $D_m = \lambda/\chi_m$ . Deep within the spiral state, where the magnetization is parameterized by  $\phi = |\psi_0|e^{i\varphi+iq_1x_a}$  and  $\psi_0$  can be taken to be a constant, the hydrodynamic equations reduce further to linear coupled equations for the Goldstone mode  $\varphi(\mathbf{r})$  and its conjugate  $a$ -component of the magnetization,  $m(\mathbf{r})$

$$\partial_t \varphi = -\gamma \tilde{\epsilon}_0 \varphi - \Gamma m / \chi_m + \zeta_\varphi \quad (66a)$$

$$\partial_t m = D_m \nabla^2 m + \Gamma |\psi_0|^2 \tilde{\epsilon}_0 \varphi + \zeta_m \quad (66b)$$

with  $\tilde{\epsilon}_0 = -c_a \partial_a^2 - c_b \partial_b^2$ , and  $\zeta_\varphi = \text{Re}[-i\zeta e^{-iq_1x_a}]/|\psi_0|$ . These strongly resemble model-E hydrodynamics, appropriate for our planar magnetic system,<sup>19</sup> with the noise  $\zeta_\varphi$  governed by a zero-mean Gaussian statistics, characterized by

$$\langle \zeta_\varphi(\mathbf{r}, t) \zeta_\varphi(\mathbf{r}', t') \rangle = 2\gamma k_B T \delta(\mathbf{r} - \mathbf{r}') \delta(t - t') / |\psi_0|^2 \quad (67)$$

After Fourier transform, we obtain,

$$\begin{pmatrix} \varphi_{\mathbf{k}, \omega} \\ m_{\mathbf{k}, \omega} \end{pmatrix} \simeq (-\omega^2 + \Omega_{\mathbf{k}}^2 - i\omega D_{\mathbf{k}} k^2)^{-1} \begin{pmatrix} -i\omega + D_m k^2 & -\Gamma/\chi_m \\ \Gamma |\psi_0|^2 \tilde{\epsilon}_{0, \mathbf{k}} & -i\omega + \gamma \tilde{\epsilon}_{0, \mathbf{k}} \end{pmatrix} \begin{pmatrix} \zeta_{\mathbf{k}, \omega}^\varphi \\ \zeta_{\mathbf{k}, \omega}^m \end{pmatrix} \quad (68)$$

with  $\tilde{\epsilon}_{0, \mathbf{k}} = c_a k_a^2 + c_b k_b^2$ , and

$$\Omega_{\mathbf{k}} = (\Gamma^2 |\psi_0|^2 / \chi_m + \gamma D_m k^2)^{1/2} \tilde{\epsilon}_{0, \mathbf{k}}^{1/2}, \quad (69a)$$

$$D_{\mathbf{k}} = \gamma \tilde{\epsilon}_{0, \mathbf{k}} / k^2 + D_m. \quad (69b)$$

The poles of the above transfer function (zeros of the characteristic equation) give the spectrum in the incommensurate spiral state

$$\omega_{\mathbf{k}} = -\frac{i}{2}(\gamma \tilde{\epsilon}_{0, \mathbf{k}} + D_m k^2) \pm \frac{1}{2} [ -(\gamma \tilde{\epsilon}_{0, \mathbf{k}} + D_m k^2)^2 + 4D_m \gamma \tilde{\epsilon}_{0, \mathbf{k}} k^2 + 4\Gamma^2 |\psi_0|^2 \tilde{\epsilon}_{0, \mathbf{k}} / \chi_m ]^{1/2} \quad (70a)$$

$$\simeq \pm \Gamma \sqrt{|\psi_0|^2 \tilde{\epsilon}_{0, \mathbf{k}} / \chi_m - \frac{1}{2} i(\gamma \tilde{\epsilon}_{0, \mathbf{k}} + D_m k^2)} \quad (70b)$$

$$\simeq \pm \Omega_{\mathbf{k}} - \frac{i}{2} D_{\mathbf{k}} k^2 \quad (70c)$$

$$\simeq \pm v_{\mathbf{k}} k - \frac{i}{2} D_{\mathbf{k}} k^2 \quad (70d)$$

where  $\Omega_{\mathbf{k}} \approx \Gamma |\psi_0| \sqrt{\tilde{\epsilon}_{0, \mathbf{k}} / \chi_m} \equiv v_{\mathbf{k}} k$ .

Averaging over noise of Eq. (67), we obtain correlation functions which are defined in the following form,

$$\langle \varphi_{\mathbf{k}, \omega} \varphi_{\mathbf{k}', \omega'} \rangle = C_{\varphi\varphi}(\mathbf{k}, \omega) (2\pi)^3 \delta(\mathbf{k} + \mathbf{k}') \delta(\omega + \omega'), \quad (71)$$

and

$$C_{\varphi\varphi} \simeq \frac{2k_B T (\gamma \omega^2 / |\psi_0|^2 + \lambda \Gamma^2 k^2 / \chi_m^2)}{(\omega^2 - \Omega_{\mathbf{k}}^2)^2 + \omega^2 (D_{\mathbf{k}} k^2)^2} \quad (72a)$$

$$C_{mm} \simeq \frac{2k_B T (\gamma \Gamma^2 |\psi_0|^2 \tilde{\epsilon}_{0, \mathbf{k}}^2 + \lambda \omega^2 k^2)}{(\omega^2 - \Omega_{\mathbf{k}}^2)^2 + \omega^2 (D_{\mathbf{k}} k^2)^2} \quad (72b)$$

$$C_{\varphi m} \simeq \frac{-i 2k_B T \Gamma \omega D_{\mathbf{k}} k^2}{(\omega^2 - \Omega_{\mathbf{k}}^2)^2 + \omega^2 (D_{\mathbf{k}} k^2)^2}, \quad (72c)$$

where above we neglected terms that are subdominant in the long-wavelength, low-frequency limit. We note that these correlation functions are quite similar to those of the planar uniform magnet obtained in Ref. 19. This is despite the fact that here the ordered state is a *periodic* planar spiral. Nevertheless, because in this state the conjugate field  $m$  (the  $a$ -component of the magnetization) remains uniform, vanishing on average and locally conserved (as in uniform magnetic states), its hydrodynamics is qualitatively identical to that of an easy-plane ferromagnet and a superfluid (model E).

## 2. Commensurate phase

We now apply above analysis to the commensurate state, where the pinning anisotropy arising from the orthorhombic distortion plays an important role. Its main consequence is pinning of the spiral at a wavevector  $q_0$  commensurate with the lattice, orienting spins along the  $b$ -axis and thereby opening the gap in the spin wave spectrum.

By definition, deep in the commensurate phase the pinning is strong, with the equation of motion given by

$$\partial_t \varphi = -\gamma \tilde{\epsilon}_0 \varphi - \Gamma m / \chi_m - 2\gamma D_{bc} \sin(2\varphi - 2Qx_a) + \zeta_\varphi \quad (73a)$$

$$\partial_t m = D_m \nabla^2 m + \Gamma |\psi_0|^2 \tilde{\epsilon}_0 \varphi + 2\Gamma D_{bc} |\psi_0|^2 \sin(2\varphi - 2Qx_a) + \zeta_m. \quad (73b)$$

We change variables using  $\theta = Qx_a - \varphi$ , as defined by Eq.(39), and use the fact that in the commensurate state the sine-Gordon nonlinearity is strong, forcing  $\theta$  to fluctuate about 0. Thus in this phase, the dynamics is well captured by a linear approximation in  $\theta$

$$\partial_t \theta = -\gamma (\tilde{\epsilon}_0 + 4D_{bc}) \theta + \Gamma m / \chi_m - \zeta_\varphi \quad (74a)$$

$$\partial_t m = D_m \nabla^2 m - \Gamma |\psi_0|^2 (\tilde{\epsilon}_0 + 4D_{bc}) \theta + \zeta_m, \quad (74b)$$

allowing us to straightforwardly compute the hydrodynamic correlation functions. Fourier transforming, we find

$$\begin{pmatrix} \theta_{\mathbf{k},\omega} \\ m_{\mathbf{k},\omega} \end{pmatrix} = (-\omega^2 + \tilde{\Omega}_{\mathbf{k}}^2 - i\omega \tilde{D}_{\mathbf{k}} k^2)^{-1} \begin{pmatrix} -i\omega + D_m k^2 & \Gamma / \chi_m \\ -\Gamma |\psi_0|^2 (\tilde{\epsilon}_{0,\mathbf{k}} + 4D_{bc}) & -i\omega + \gamma (\tilde{\epsilon}_{0,\mathbf{k}} + 4D_{bc}) \end{pmatrix} \begin{pmatrix} -\zeta_{\mathbf{k},\omega}^\varphi \\ \zeta_{\mathbf{k},\omega}^m \end{pmatrix} \quad (75)$$

where  $\tilde{D}_{\mathbf{k}} = \gamma (\tilde{\epsilon}_{0,\mathbf{k}} + 4D_{bc}) / k^2 + D_m$ ,  $\tilde{\Omega}_{\mathbf{k}} = \tilde{v}_{\mathbf{k}} (\tilde{\epsilon}_{0,\mathbf{k}} + 4D_{bc})^{1/2}$  and  $\tilde{v}_{\mathbf{k}} = (\Gamma^2 |\psi_0|^2 / \chi_m + \gamma D_m k^2)^{1/2} \approx \Gamma |\psi_0| / \sqrt{\chi_m}$ .

Using Gaussian noise statistics (Eqs. (57a),(57b)) to average over  $\zeta_\varphi$  and  $\zeta_m$ , we obtain

$$C_{\theta\theta} \simeq \frac{2k_B T (\gamma \omega^2 + D_m \tilde{v}_{\mathbf{k}}^2 k^2) / |\psi_0|^2}{(\omega^2 - \tilde{\Omega}_{\mathbf{k}}^2)^2 + \omega^2 \Delta_{\mathbf{k}}^2} \quad (76a)$$

$$C_{mm} \simeq \frac{2k_B T \chi_m [\gamma (\tilde{\epsilon}_{0,\mathbf{k}} + 4D_{bc}) \tilde{\Omega}_{\mathbf{k}}^2 + D_m \omega^2 k^2]}{(\omega^2 - \tilde{\Omega}_{\mathbf{k}}^2)^2 + \omega^2 \Delta_{\mathbf{k}}^2} \quad (76b)$$

$$C_{\theta m} \simeq \frac{i2k_B T \Gamma \omega \Delta_{\mathbf{k}}}{(\omega^2 - \tilde{\Omega}_{\mathbf{k}}^2)^2 + \omega^2 \Delta_{\mathbf{k}}^2}, \quad (76c)$$

where  $\Delta_{\mathbf{k}} \equiv \tilde{D}_{\mathbf{k}} k^2 \simeq 4\gamma D_{bc}$  and we neglected terms that are subdominant in the long-wavelength, low-frequency limit.

We note, that as anticipated, in contrast to the incommensurate phase of the previous subsection, here, inside the commensurate state we find a gapful spectrum, set by the single-ion anisotropy  $D_{bc}$ . This is consistent with the microscopic spin-wave analysis of Sec. II and with experimental observations.<sup>18</sup>

## VI. SUMMARY

In this work, we formulated an  $S = 1$  exchange model of magnetic and structural ordering in  $\text{Fe}_{1+y}\text{Te}$ , a simplest parent compound of Fe-based high-temperature superconductor. In addition to the exchange,<sup>9</sup> we incorporated a competing ingredient of single-ion orthorhombic

anisotropy. We demonstrated that this model exhibits experimentally observed commensurate bicollinear AFM and incommensurate spiral states, mapped out the corresponding zero temperature phase diagram and a low energy spin-wave excitation spectra, latter predicted to be gapped (consistent with experiments) in the commensurate bicollinear AFM state.

To understand the interplay between observed tetragonal-orthorhombic structural distortion and spiral order transitions at finite temperatures, starting with this microscopic description we derived an effective Landau theory and used it to qualitatively map out the temperature-doping phase diagram. Generalizing it to hydrodynamics, that falls in the variant of the model E universality class of Hohenberg-Halperin classification,<sup>19,20</sup> we computed the static and dynamic structure functions  $S(\mathbf{q},\omega)$  in the PM, commensurate bicollinear AFM and incommensurate spiral states. The evolution of the predicted inelastic peaks with temperature and strength of the single-ion anisotropy shows qualitative features observed in the experiments, shifting from the incommensurate to commensurate positions as the ordered state is approached from the above. We hope that these predictions stimulate further systematic experimental studies of this interesting magnetic system.

## VII. ACKNOWLEDGMENTS

This work was supported by the NSF through DMR-1001240 (LR), MRSEC DMR-0820579 (LR), by DOE award DE-SC0003910 (GC). We thank D. Parshall and

D. Reznik, for sharing their experimental data before publication and discussions.

- 
- <sup>1</sup> Y. Kamihara, T. Watanabe, M. Hirano, and H. Hosono, *J. Am. Chem. Soc.* **130**, 3296 (2008)
- <sup>2</sup> J. Paglione and R. L. Greene, *Nature Physics* **6**, 645 (2010)
- <sup>3</sup> H.-J. Grafe, D. Paar, G. Lang, N. J. Curro, G. Behr, J. Werner, J. Hamann-Borrero, C. Hess, N. Leps, R. Klingeler, and B. Büchner, *Phys. Rev. Lett.* **101**, 047003 (2008)
- <sup>4</sup> C.-T. Chen, C. C. Tsuei, M. B. Ketchen, Z.-A. Ren, and Z. X. Zhao, *Nature Physics* **6**, 260 (2010)
- <sup>5</sup> W. Bao, Y. Qiu, Q. Huang, M. A. Green, P. Zajdel, M. R. Fitzsimmons, M. Zhernenkov, S. Chang, M. Fang, B. Qian, E. K. Vehstedt, J. Yang, H. M. Pham, L. Spinu, and Z. Q. Mao, *Phys. Rev. Lett.* **102**, 247001 (2009)
- <sup>6</sup> S. Li, C. de la Cruz, Q. Huang, Y. Chen, J. W. Lynn, J. Hu, Y.-L. Huang, F.-C. Hsu, K.-W. Yeh, M.-K. Wu, and P. Dai, *Phys. Rev. B* **79**, 054503 (2009)
- <sup>7</sup> A. Subedi, L. Zhang, D. J. Singh, and M. H. Du, *Phys. Rev. B* **78**, 134514 (2008)
- <sup>8</sup> Y. Xia, D. Qian, L. Wray, D. Hsieh, G. F. Chen, J. L. Luo, N. L. Wang, and M. Z. Hasan, *Phys. Rev. Lett.* **103**, 037002 (2009)
- <sup>9</sup> A. M. Turner, F. Wang, and A. Vishwanath, *Phys. Rev. B* **80**, 224504 (2009)
- <sup>10</sup> C. Fang, B. A. Bernevig, and J. Hu, *Europhys. Lett.* **86**, 67005 (2009)
- <sup>11</sup> L. Zhang, D. Singh, and M. Du, *Phys. Rev. B* **79**, 012506 (2009)
- <sup>12</sup> F. Ma, W. Ji, J. Hu, Z. Y. Lu, and T. Xiang, *Phys. Rev. Lett.* **102**, 177003 (2009)
- <sup>13</sup> W. G. Yin, C. C. Lee, and W. Ku, *Phys. Rev. Lett.* **105**, 107004 (2010)
- <sup>14</sup> C. Şen, G. Alvarez, and E. Dagotto, *Phys. Rev. Lett.* **98**, 127202 (2007)
- <sup>15</sup> C. Stock, E. E. Rodriguez, M. A. Green, P. Zavalij, and J. A. Rodriguez-Rivera, *Phys. Rev. B* **84**, 045124 (2011)
- <sup>16</sup> O. J. Lipscombe, G. F. Chen, T. G. Perring, D. L. Abernathy, A. D. Christianson, T. Egami, N. Wang, J. Hu, and P. Dai, *Phys. Rev. Lett.* **106**, 057004 (2011)
- <sup>17</sup> E. E. Rodriguez, C. Stock, P. Zajdel, K. L. Krycka, C. F. Majkrzak, P. Zavalij, and M. A. Green, *Phys. Rev. B* **84**, 064403 (2011)
- <sup>18</sup> D. Parshall, G. Chen, L. Pintschovius, D. Lamago, T. Wolf, L. Radzihovsky, and D. Reznik, *Phys. Rev. B* **85**, 140515 (Apr 2012)
- <sup>19</sup> B. I. Halperin and P. C. Hohenberg, *Phys. Rev.* **188**, 898 (1969)
- <sup>20</sup> P. C. Hohenberg and B. I. Halperin, *Rev. Mod. Phys.* **49**, 435 (1977)
- <sup>21</sup> L. Messio, C. Lhuillier, and G. Misguich, *Phys. Rev. B* **83**, 184401 (2011)
- <sup>22</sup> I. Paul, A. Cano, and K. Sengupta, *Phys. Rev. B* **83**, 115109 (2011)
- <sup>23</sup> V. Pokrovsky, A. L. Talapov, and P. Bak, in *Solitons*, edited by S. E. Trullinger, V. E. Zakharov and V. L. Pokrovsky (North Holland, Amsterdam, 1986).
- <sup>24</sup> M. G. Kim, R. M. Fernandes, A. Kreyssig, J. W. Kim, A. Thaler, S. L. Bud'ko, P. C. Canfield, R. J. McQueeney, J. Schmalian, and A. I. Goldman, *Phys. Rev. B* **83**, 134522 (Apr 2011)
- <sup>25</sup> K. Prokeš, S. Mat'aš, L. Harnagea, S. Singh, S. Wurmehl, D. N. Argyriou, and B. Büchner, *Phys. Rev. B* **83**, 104414 (Mar 2011)